Soft Matter

PAPER

View Article Online
View Journal | View Issue

Cite this: *Soft Matter*, 2024, **20**, 4795

Influence of bacterial swimming and hydrodynamics on attachment of phages†

Christoph Lohrmann, [a] Christian Holm [b] and Sujit S. Datta *[c]

Bacteriophages ("phages") are viruses that infect bacteria. Since they do not actively self-propel, phages rely on thermal diffusion to find target cells—but can also be advected by fluid flows, such as those generated by motile bacteria themselves in bulk fluids. How does the flow field generated by a swimming bacterium influence how it encounters phages? Here, we address this question using coupled molecular dynamics and lattice Boltzmann simulations of flagellated bacteria swimming through a bulk fluid containing uniformly-dispersed phages. We find that while swimming increases the rate at which phages attach to both the cell body and flagellar propeller, hydrodynamic interactions strongly suppress this increase at the cell body, but conversely enhance this increase at the flagellar bundle. Our results highlight the pivotal influence of hydrodynamics on the interactions between bacteria and phages, as well as other diffusible species, in microbial environments.

Received 15th January 2024,
Accepted 30th May 2024

DOI: 10.1039/d4sm00060a

rsc.li/soft-matter-journal

1 Introduction

More than 10^{31} bacteriophages ("phages" for short) are estimated to exist on Earth, more than every other organism on the planet combined.[1,2] Indeed, on average, phages—viruses that infect bacteria—outnumber bacterial cells by a factor of ten.[3] Thus, their interactions with phages regulate how bacteria function in natural environments, with critical implications for agriculture, ecology, and medicine.[4–8] Extensive research has focused on documenting various biological and chemical factors that influence these interactions; nevertheless, the basic physical processes underlying how bacteria encounter and ultimately become infected by phages in the first place remain poorly understood.

For example: while phages do not actively self-propel, many bacteria do using, *e.g.*, flagella-driven swimming through fluids. We therefore focus on this mode of motility here. How does swimming influence the rate at which bacteria encounter and eventually become infected by phages, if at all? Despite its apparent simplicity, this question still does not have a clear answer[9]—even for the illustrative, idealized case of a cell swimming at a constant velocity v_{swim} in an unbounded, uniform, Newtonian fluid at low Reynolds number. One might expect that the rate at which phages encounter and attach to the cell simply increases proportionately with its swimming speed as it explores more space;[10] however, this expectation does not consider the complex flow field generated by the bacterium around itself as it swims,[11] which can advect and entrain surrounding phages in a non-trivial manner.[11,12] The importance of these hydrodynamics is highlighted by examining the Péclet number comparing the characteristic rates of phage transport by fluid advection and thermal diffusion, $\mathrm{Pe}_{\mathrm{phage}} \equiv v_{\mathrm{swim}} r_{\mathrm{body}}/D^{\mathrm{P}}$, which exceeds unity for typical values of the bacterial swimming speed $v_{\mathrm{swim}} \sim$ 10–100 μm s^{-1}, size $r_{\mathrm{body}} \sim 1$ μm, and phage diffusivity $D^{\mathrm{P}} \sim$ 1–10 $\mu\mathrm{m}^2\ \mathrm{s}^{-1}$. Hence, the rate at which phages encounter, attach to, and ultimately infect a bacterium is likely highly sensitive to the nature of the flow field it generates by swimming.

In a classic study,[13] Berg and Purcell examined the influence of these hydrodynamics by treating the swimming bacterium as an externally-driven sphere. Building on prior calculations,[14,15] the authors concluded that because the cell pushes fluid around it as it moves, "motility cannot significantly increase the cell's acquisition of material". While this study focused on cellular interactions with chemical species like nutrients, the authors considered interactions with phages as a specific application of their results—concluding that the phage attachment rate only increases sublinearly with swimming speed. However, while instructive, this analysis neglects two crucial features of flagellated bacteria—which are not uniform spheres, but are typically comprised of an elongated cell body driven by an adjoined elongated flagellar propeller. First, it is now well known that many such bacteria (including *Escherichia coli*, *Bacillus subtilis*, and *Salmonella enterica*) are force-free "pushers": each cell pushes on surrounding fluid with an equal and opposite force to the one generated by its flagella as it swims.[11,16,17] As a result, the fluid

[a] *Institute for Computational Physics, University of Stuttgart, 70569 Stuttgart, Germany. E-mail: clohrmann@icp.uni-stuttgart.de*
[b] *Institute for Computational Physics, University of Stuttgart, 70569 Stuttgart, Germany. E-mail: holm@icp.uni-stuttgart.de*
[c] *Department of Chemical and Biological Engineering, Princeton University, Princeton, New Jersey 08544, USA. E-mail: ssdatta@princeton.edu*

† Electronic supplementary information (ESI) available. See DOI: https://doi.org/10.1039/d4sm00060a

boundary conditions are distinct for the cell body and the flagella, and phage attachment rates may thus differ considerably between the two. Second, the flow field away from such a swimming bacterium has a dipolar shape with a fluid velocity magnitude v that decays with distance r away from the cell as $\sim 1/r^2$, unlike the longer-ranged $v(r) \sim 1/r$ decay characteristic of a driven sphere. How these two features influence the manner in which phages encounter and attach to swimming bacteria is, to the best of our knowledge, still unknown.

Here, we address this gap in knowledge using simulations of a bacterium swimming through a fluid containing uniformly-dispersed phages. We focus on the case of ''pusher''-type bacteria in the main text; we find qualitatively similar results for the opposite case of ''pullers'', as detailed in the ESI.† We use particle-resolved molecular dynamics to explicitly treat the cell body, flagellar propeller (hereafter referred to as the flagellum for convenience), and individual phages, all of which are coupled to and interact *via* an underlying fluid which we simulate using a lattice Boltzmann algorithm. We find that while bacterial swimming increases the rate at which the phages attach to the cell body, the dipolar flow thereby generated advects phages away from the forward-facing ''head'' of the cell body, thereby suppressing this increase by as much as twofold—as suggested by Berg and Purcell. However, this dipolar flow field also pumps phage-containing fluid to the flagellum. As a result, the phage attachment rate at the flagellum is appreciable and increases nearly linearly with swimming speed, in stark contrast to the findings of Berg and Purcell. Altogether, our work suggests that while the fluid flow generated by swimming helps to protect the bacterial cell body from phages, it promotes phage attachment at the flagellum—an effect that, to the best of our knowledge, has been overlooked in previous work. This effect may be exploited by flagellotropic phages, *i.e.*, phages that initiate infection by attaching to the host flagellum, which are increasingly being recognized as key constituents of natural microbial communities and potentially useful therapeutics against pathogenic bacteria.[18,19] More broadly, our findings highlight the pivotal influence of hydrodynamics on the interactions between bacteria and phages, as well as other diffusible species, in microbial environments.

2 Methods

2.1 Molecular dynamics model of phages and bacterium

We use a particle-resolved, coarse-grained molecular dynamics algorithm to represent the phages and bacterium. Particles of each are coupled to and interact with each other *via* an underlying lattice Boltzmann fluid through friction forces, as detailed below. This approach enables us to simulate the coupling between short-range interactions between phage and bacteria and larger-range hydrodynamic interactions associated with bacterial swimming. While here we focus on the case of a Newtonian fluid, which is relevant to many aquatic microbial habitats, studying the case of a more complex non-Newtonian fluid[10,20–31] will be a useful extension of our work.

Phages. For simplicity, we treat phages as uniform spherical particles. Their dynamics in three spatial dimensions are described by the Langevin equations

$$m^{\mathrm{P}}\ddot{\mathbf{r}}_i^{\mathrm{P}} = \mathbf{F}_i^{\text{phage–fluid}} + \mathbf{F}_i^{\text{bact–phage}}, \tag{1}$$

where

$$\mathbf{F}_i^{\text{phage–fluid}} = -\gamma^{\mathrm{P}*}\left[\dot{\mathbf{r}}_i^{\mathrm{P}} - \mathbf{v}_{\mathrm{fl}}\left(\mathbf{r}_i^{\mathrm{P}}\right)\right] + \sqrt{2\gamma^{\mathrm{P}*}k_{\mathrm{B}}T}\boldsymbol{\eta}_i^{\mathrm{P}}(t); \tag{2}$$

Here, m^{P} denotes the phage mass, $\mathbf{r}^{\mathrm{P}}$ the phage position, i the particle index, the overdot a derivative with respect to time, $\gamma^{\mathrm{P}*}$ the phage–fluid friction coefficient, $\mathbf{v}_{\mathrm{fl}}$ the fluid velocity, k_{B} Boltzmann's constant, T the temperature, $\boldsymbol{\eta}^{\mathrm{P}}$ a noise term, and $\mathbf{F}^{\text{bact–phage}}$ the phage–bacterium interaction force. The noise term has mean $\langle\eta^{\mathrm{P}}\rangle = \mathbf{0}$ and correlations $\langle\eta_i^{\mathrm{P}}(t)\eta_j^{\mathrm{P}}(t')\rangle = \delta_{ij}\delta(t-t')\mathbf{1}$, where $\langle\cdot\rangle$ denotes an ensemble average and $\mathbf{1}$ the identity matrix in three dimensions. Our focus here is on phage–bacteria encounters, and we therefore do not consider any phage–phage interactions.

We treat hydrodynamics at a continuum level by solving the Navier–Stokes equations using a standard two-relaxation time lattice Boltzmann algorithm with ''magic'' parameter $\Lambda = 3/16$ and Guo forcing.[32] Thermal fluctuations of the fluid are included following the approach of ref. 33. To obtain the fluid velocity $\mathbf{v}_{\mathrm{fl}}$ at the particle positions $\mathbf{r}_i^{\mathrm{P}}$, we interpolate between the nearest lattice nodes according to ref. 34. The coupling force $\mathbf{F}^{\text{phage–fluid}}$ reflects the microscopic interactions between the fluid and the phage particles. These interactions obey Newton's third law, so the coupling force is also applied to the fluid, but with opposite sign. We thus extrapolate $-\mathbf{F}^{\text{phage–fluid}}$ to the nearest lattice node as detailed in ref. 34.

Bacterium. Our model for the bacterium builds on previous studies of microswimmers,[35–38] extended to also explicitly consider the cell and flagellum geometry. Specifically, we represent the bacterium by a rigid collection of three different types of particles denoted by τ to model the rod-like shape of flagellated bacteria like *E. coli*, *B. subtilis*, and *S. enterica*. The first type of spheres (large green spheres in Fig. 1) define the volume of the cell body through the almost-hard-sphere potential given in eqn (10) detailed below. They therefore mediate close-range interactions between the cell body and phage particles, but do not incorporate the appropriate hydrodynamic boundary conditions since these spheres only experience point-friction with the fluid at their center. The second type of spheres (smaller green spheres in Fig. 1) address this issue; they only experience friction with the fluid on the cell surface, and therefore incorporate the no-slip boundary condition that is a key characteristic of the cell body surface. However, these second spheres take up no volume and therefore do not otherwise interact with phages. The third type (medium blue spheres in Fig. 1) consists of spheres that make up the flagellum. Similar to the first type, they interact with phages *via* an almost-hard-sphere potential. However, unlike those comprising the cell body, these particles do not experience friction with the fluid. Instead, they exert a force on the fluid that is equal in magnitude but opposite in sign to the swim force $\mathbf{F}^{\text{swim}}$ that propels the cell body forward, ensuring that the overall

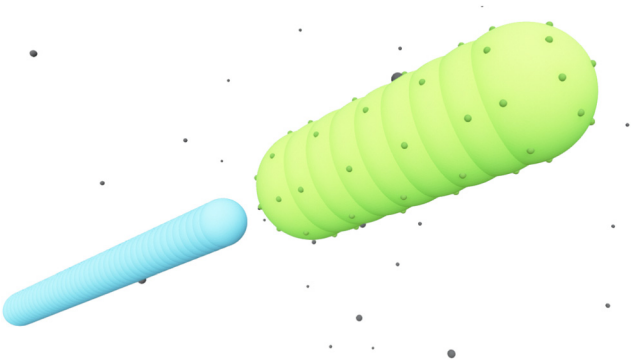

Fig. 1 Rendering of our rigid-body, coarse-grained molecular dynamics model of a swimming bacterium. Large green and medium blue spheres define the volume of the cell body and flagellum, respectively, thereby mediating close-ranged phage–bacteria interactions. Small, darker green spheres mark the locations of particle–fluid coupling points that do not directly interact with phages but instead approximate a no-slip fluid boundary condition at the surface of the cell. Small gray spheres represent phages dispersed in the surrounding fluid.

swimming bacterium is net force-free. This model represents a coarse-grained picture of a swimming bacterium that does not take into account the helical geometry of a flagellum or the intricate inner structure of a flagellar bundle, and does not specify the exact mechanism by which the propulsion force is generated or how the fluid is pushed through the flagellar bundle. Instead, we take a coarser-grained view of propulsion that incorporates the essential feature of this form of microswimming: that fluid is pushed backwards through the flagellar bundle, creating a forward force on the cell body that propels the cell forward. While in reality the filaments in a flagellar bundle have no fluid slip at their individual surfaces, at the coarse-grained level appropriate for our hydrodynamic simulations, the entire flagellar bundle must be treated with a different boundary condition given that fluid can move through the bundle as shown in experiments.[11] Thus, in short, our model is designed to capture four essential features of the bacterial flagellar propeller: it is permeable to fluid, exerts a force on the fluid, occupies a non-zero volume, and crucially, phages can attach to it.

More specifically, the cell body comprises N^{body} particles of type one arranged in a line along $\hat{\mathbf{e}}$, evenly spaced over the length l_{body}, along with N^{coupl} additional coupling points of type two on the surface of the cell body. The dynamics of the central particle of the cell body in three spatial dimensions are described by the equations of motion

$$m^{\mathrm{B}}\ddot{\mathbf{r}}^{\mathrm{B}} = \mathbf{F}^{\mathrm{bact-fluid}} + \mathbf{F}^{\mathrm{swim}} + \sum_i \mathbf{F}_i^{\mathrm{bact-phage}} \tag{3}$$

for the center of mass position and

$$\dot{\hat{\mathbf{e}}} = \omega \times \hat{\mathbf{e}}, \tag{4}$$

$$I\dot{\omega} = \mathbf{M}^{\mathrm{bact-fluid}} + \sum_i \mathbf{M}_i^{\mathrm{bact-phage}} \tag{5}$$

for the orientation; here, m^{B} denotes the mass of the cell, $\mathbf{r}^{\mathrm{B}}$ its position, $\mathbf{F}^{\mathrm{swim}} \equiv F^{\mathrm{swim}}\hat{\mathbf{e}}$ the swim force of magnitude F^{swim} and orientation $\hat{\mathbf{e}}$, ω the angular velocity, I the moment of inertia tensor, and the summation runs over all phage particles i. All other particles add their forces and torques to the central particle, themselves following its trajectory in their predefined relative position and orientation to keep the shape of the rigid bacterium. The resulting coupling force is given by

$$\mathbf{F}^{\mathrm{bact-fluid}} = \sum_{j|\tau_j\in\{1,2\}} \mathbf{F}_j^{\mathrm{bact-fluid}}, \tag{6}$$

where the summation runs over all particles j with type τ_j associated with the cell body. The individual coupling forces are calculated analogous to eqn (2):

$$\mathbf{F}_j^{\mathrm{bact-fluid}} = -\tilde{\gamma}^{\mathrm{B}}\left[\dot{\mathbf{r}}_j^{\mathrm{B}} - \mathbf{v}_{\mathrm{fl}}\left(\mathbf{r}_j^{\mathrm{B}}\right)\right] + \sqrt{2\tilde{\gamma}^{\mathrm{B}}k_{\mathrm{B}}T}\boldsymbol{\eta}_j^{\mathrm{B}}(t), \tag{7}$$

where $\mathbf{r}_j^{\mathrm{B}}$ denotes the position of the jth particle of the cell body, $\tilde{\gamma}^{\mathrm{B}}$ the bare friction coefficient, and $\boldsymbol{\eta}_j^{\mathrm{B}}$ a noise term with the same properties as η^{P}. As for the phages, all coupling forces $\mathbf{F}_j^{\text{bact-fluid}}$ are also applied to the fluid in the opposite direction to ensure net momentum conservation. The coupling forces also lead to the torque

$$\mathbf{M}^{\mathrm{bact-fluid}} = \sum_j \left(\mathbf{r}_j^{\mathrm{B}} - \mathbf{r}^{\mathrm{B}}\right) \times \mathbf{F}_j^{\mathrm{bact-fluid}}. \tag{8}$$

The flagellum is modelled by $N^{\mathrm{flagellum}}$ particles of type three arranged in a line along $\hat{\mathbf{e}}$ and evenly spaced over a length l_{flag}, with the central particle of the flagellum at a distance l_{dipole} behind the central particle of the cell body. Flagellum particles do not experience friction or noise as the other particles in the system. Instead, each of them applies a force

$$\mathbf{F}_j^{\mathrm{flagellum}} = -\frac{F^{\mathrm{swim}}}{N^{\mathrm{flagellum}}}\hat{\mathbf{e}} \tag{9}$$

to the fluid, such that the forward force on the bacterium is balanced by a backward force on the fluid and the total force resulting from bacterial swimming is zero.

Cell body particles of type one and flagellum particles interact with phages *via* the short-ranged, purely-repulsive, almost-hard-sphere Weeks–Chandler–Anderson potential[39]

$$V_{ij}(r_{ij}) = 4\varepsilon\left[\left(\frac{\sigma_i}{r_{ij}}\right)^{12} - \left(\frac{\sigma_i}{r_{ij}}\right)^{6} + \varepsilon\right] H\left(2^{1/6}\sigma_i - r_{ij}\right); \tag{10}$$

here, $r_{ij} = |\mathbf{r}_i^{\mathrm{P}} - \mathbf{r}_j^{\mathrm{B}}|$ is the distance between bacterium particle j and phage i, ε the interaction strength, and $H(\cdot)$ the Heaviside step-function. We choose $\varepsilon = 10k_{\mathrm{B}}T$ to limit overlap between particles. The scale parameter σ_i depends on the types of particles involved. For cell body particles of type one, it is given by $\sigma_i = 2^{-1/6}(r_{\mathrm{body}} + r^{\mathrm{P}})$, while for flagellum particles, it is given by $\sigma_i = 2^{-1/6}(r_{\mathrm{flag}} + r^{\mathrm{P}})$, where r_{body}, r_{flag}, and r^{P} are the radii of the cell body, the flagellum, and the phages, respectively. Forces and torques are then given by the gradient of this potential:

$$\mathbf{F}_i^{\text{bact-phage}} = \sum_j -\nabla V_{ij}, \tag{11}$$

$$\mathbf{M}_i^{\text{bact-phage}} = \sum_j (\mathbf{r}_j^{\text{B}} - \mathbf{r}^{\text{B}}) \times \nabla V_{ij}. \quad (12)$$

In our simulations, we solve eqn (1)–(12) numerically using the development version of the ESPResSo simulation package[40] with the waLBerla[41,42] library for lattice Boltzmann hydrodynamics. Exact software versions as well as our custom code are freely available; details are provided in ref. 43.

Simulations without hydrodynamics. As a further test of the influence of hydrodynamics, we also perform simulations that do not include the hydrodynamic field. For the phage particles, we set $\mathbf{v}_{\text{fl}}(\mathbf{r}^{\text{P}}) = \mathbf{0}$. For the bacterium, the equations further simplify, because we do not introduce the additional coupling particles of type two. Instead, we have $\mathbf{F}^{\text{bact-fluid}} = -\gamma_{\text{t}}^{\text{B}}\dot{\mathbf{r}}^{\text{B}} + \sqrt{2\gamma_{\text{t}}^{\text{B}} k_{\text{B}} T}\eta_{\text{t}}^{\text{B}}(t)$ and $\mathbf{M}^{\text{bact-fluid}} = -\gamma_{\text{r}}^{\text{B}}\omega + \sqrt{2\gamma_{\text{r}}^{\text{B}} k_{\text{B}} T}\eta_{\text{r}}^{\text{B}}(t)$, where $\gamma_{\text{t}}^{\text{B}}$ and $\gamma_{\text{r}}^{\text{B}}$ are the translational and rotational friction coefficients, respectively.

2.2 Model of phage attachment

We consider a phage as being in contact with the bacterium (either the cell body or flagellum) if the surface-to-surface distance is smaller than a prescribed encounter distance d_{enc}. Once it contacts the bacterium, the phage attaches to the cell at a rate k^{att}, which is a lumped parameter that reflects the influence of short-ranged microscopic interactions mediating the complex process of binding to specific receptors to complete the process of attachment.[44,45] As we show below, the overall qualitative insights that result from our simulations are insensitive to the specific choice of k^{att}. Because our focus is on the purely physical processes underlying phage encounter and attachment, we do not consider the subsequent biological steps needed for the phage to actually insert its genetic material into the cell and complete the process of infection.

In our time-discretised numerical implementation, we check for phages in contact with the bacterium after every successive time interval Δt. For such contacting phages, we calculate the attachment probability $p^{\text{att}} = \Delta t k^{\text{att}}$. Based on this probability, using a random number generator, we choose whether the phage remains free or it successfully attaches to the cell. If attachment happens, we register the time and relative position of the phage encounter on the bacterium surface. We then move the phage to a random position outside the encounter region defined by d_{enc} to prevent double-counting; this procedure mimics the case of a bacterium swimming in an infinite fluid reservoir with constant phage number density.

We apply the same model for phage attachment to both the cell body and the flagellar bundle. We thus use contact with the flagellar bundle as the criterion for attachment instead of contact to individual flagella, which are not explicitly resolved in our coarse-grained approach. This simplifying assumption is justified because the fast motion of individual flagella, the complex flow field inside the bundle and the large surface-to-volume ratio of flagella all promote contact with phages once they have entered the bundle, making the approach to the bundle the limiting step.

We determine the overall attachment rate $J = \lim_{t\to\infty} \frac{N^{\text{att}}(t)}{t}$ from a linear fit to the computed number of phages that have attached to the cell at time t, $N^{\text{att}}(t)$ (ESI†). For the case of $k^{\text{att}} \to 0$ ($p^{\text{att}} \to 0$), the number density of phages in the encounter region is asymptotically independent of k^{att}. Hence, J scales linearly with k^{att}, and we only need to determine the number density of phages in the encounter region. Therefore, for simulations of $k^{\text{att}} \to 0$, we compute J by tracking the trajectories of phages in the contact region to obtain their number density.

2.3 Continuum modelling

To compare the results of our particle-based simulations to those of Berg and Purcell,[13] we follow their approach and solve the continuum advection-diffusion equation

$$D^{\text{P}}\nabla^2 c(\mathbf{r}) + \mathbf{v}_{\text{Stokes}}(\mathbf{r})\cdot\nabla c(\mathbf{r}) = 0 \quad (13)$$

for the phage concentration c. As in their work, we model the bacterium as a perfectly-absorbing sphere of radius $\sqrt[3]{3r_{\text{body}}{}^2 l_{\text{body}}/4}$ in an infinite reservoir of phages, with boundary conditions $c(|\mathbf{r}| = r_{\text{eq}}) = 0$ and $c(|\mathbf{r}| \to \infty) = c_\infty$. The Stokes flow field is given by

$$\mathbf{v}_{\text{Stokes}}(\mathbf{r}) = v_{\text{r}}\mathbf{e}_{\text{r}} + v_\Theta \mathbf{e}_\Theta, \quad (14)$$

$$v_{\text{r}} = -v_{\text{swim}}\cos(\Theta)\left(1 - \frac{3r_{\text{eq}}}{2r} + \frac{r_{\text{eq}}{}^3}{2r^3}\right), \quad (15)$$

$$v_\Theta = v_{\text{swim}}\sin(\Theta)\left(1 - \frac{3r_{\text{eq}}}{4r} - \frac{r_{\text{eq}}{}^3}{4r^3}\right) \quad (16)$$

in the comoving frame of reference; here, r and Θ denote the radius and polar angle in spherical coordinates, and $\mathbf{e}_{\text{r}}$, $\mathbf{e}_\Theta$ the corresponding basis vectors. The attachment rate is then given by the flux of phages into the absorbing sphere surface Ω_{s}; we compute it directly from the solution of the concentration field *via* the relation $J_{\text{Berg}} = -D^{\text{P}}\int_{\Omega_{\text{s}}} \mathbf{e}_{\text{r}}\cdot\nabla c \,\text{d}S$.

In practice, we solve eqn (13)–(16) using a finite element algorithm[46] with the boundary condition $c(|\mathbf{r}| = R) = c_0$ with $R = 50\ \mu\text{m} \gg r_{\text{eq}}$. The finite size effects from restricting the simulation domain to this radius are negligible, and the attachment rate for $v_{\text{swim}} = 0$ obtained with finite R deviates from the analytical solution for $R \to \infty$ only by $\approx 1\%$.

2.4 Choice of numerical parameters

For the phages, we choose $r^{\text{P}} = 50$ nm, which is comparable to the size of many commonly-studied phages, including T4[47] and the flagellotropic phages χ and PBS1.[19] We calculate the phage friction coefficient from Stokes' law as $\gamma^{\text{P}} = 6\pi\mu_{\text{water}} r^{\text{P}}$, where $\mu_{\text{water}} = 1 \times 10^{-3}$ Pa s is the dynamic shear viscosity of water; the numerical friction coefficient then follows from a lattice correction given by $\gamma^{\text{P}*} = [(\gamma^{\text{P}})^{-1} - (25\mu_{\text{water}} a_{\text{grid}})^{-1}]^{-1}$, where a_{grid} is the lattice Boltzmann grid constant.[34] The phage diffusion coefficient is given by the Einstein–Smoluchowski relation $D^{\text{P}} = k_{\text{B}}T/\gamma^{\text{P}} \approx 4.4\ \mu\text{m}^2\ \text{s}^{-1}$ at our choice of $T = 300$ K, which is in good agreement with experimental measurements.[10,48]

We calculate the phage mass as $m^P = \rho^P 4/3\pi(r^P)^3$, where ρ^P is the mass density of the phage. At the low Reynolds numbers (<1) relevant to this study, inertia should not play a role. However, we use the underdamped, Langevin equations of motion eqn (1)–(12) to facilitate coupling to the fluid in our coupled molecular dynamics-lattice Boltzmann framework. Therefore, we must still include inertia while both ensuring that it does not influence the results of the simulations and does not make the simulations too computationally intensive. Our choices of density accomplish this balance. First, we note that the time scale over which momentum relaxes for phage particles of size $r = 50$ nm with a density equal to that of water, $\rho_{water} = 1000$ kg m^{-3}, is $\tau^P_{diff} = m^P/\gamma^P \approx 5.6 \times 10^{-10}$ s—much smaller than the relevant time scales of our system, again reflecting the fact that inertia is not relevant. Indeed, as long as this momentum dissipation time scale is smaller that any other time scales of the system, inertia does not play a role in the physics of the system. Therefore, we instead choose $\rho^P = 10^5\rho_{water}$ such that the momentum dissipation time scale is $\tau^P_{diff} \approx 5.6 \times 10^{-5}$ s—still small compared to the time scales we are interested in, ensuring that the resulting physics remain unchanged, but large enough to enable us to choose time steps that are 10^5 times larger, $\delta t = 3.33 \times 10^{-5}$ s, rendering the simulations computationally tractable. We confirm this expectation by directly verifying that changing the phage mass density does not affect our results, as shown in the ESI.†

To mimic the commonly-studied flagellated bacterial species *E. coli*[49] and *S. enterica*,[50] we choose $l_{body} = 3$ μm and $r_{body} = 0.5$ μm, with $N^{body} = 9$ and $N^{coupl} = 62$ to obtain a sufficiently well-resolved cell surface. The bacterial mass is approximated by $m^B = \rho^B\pi {r_{body}}^2 l_{body}$; as detailed above for the phages, the diffusive time scale for bacteria is very small and the dynamics are overdamped, so we choose $\rho^B = 5 \times 10^3\rho_{water}$. For simulations without hydrodynamics, we use a spheroidal approximation, with the translational and rotational friction coefficients γ^B_t and γ^B_r calculated following, ref. 51 and 52 respectively. The force needed to propel the bacterium with the desired velocity is then given by $F^{swim} = \gamma^B_t v_{swim}$. For simulations with hydrodynamics, we set $\tilde{\gamma}^B = 2.4 \times 10^{-9}$ kg s^{-1}, which represents the largest value that we can use without impeding numerical stability to most closely approximate a no-slip boundary condition. The relation between F^{swim} and v_{swim} is nontrivial because of the complex flow field and the many coupling points; however, empirically, we find that using $F^{swim} = \gamma^{eff} v_{swim}$ with an effective friction coefficient $\gamma^{eff} = N^{body}\tilde{\gamma}^B/0.825$ yields good agreement between the desired and actual swimming velocity, as detailed further in ESI.† The flagellum is $l_{flag} = 5$ μm long with a radius of $r_{flag} = 0.25$ μm at a distance $l_{dipole} = 5$ μm, and we take $N^{flagellum} = 41$.

The lattice Boltzmann fluid has a dynamic viscosity $\mu = \mu_{water}$ and is discretised on a grid with lattice spacing $a_{grid} = r_{body}$. Since the typical size of flow field variations is larger than the cell size and all velocities are interpolated between lattice nodes, this resolution is fine enough to resolve the flow near the bacterium surface. To keep simulations stable, we choose a fluid mass density of $\rho_{fluid} = 1200\rho_{water}$. This choice does not change the flow behaviour with respect to water since the Reynolds number $Re \equiv \rho_{fluid} v_{swim} r_{body}/\mu \approx 0.017$ for a typical swimming velocity $v_{swim} = 25$ μm s^{-1} is much smaller than unity, even for this increased density. We confirm this expectation by directly verifying that changing the fluid mass density does not affect our results, as shown in the ESI.†

Our simulations consider one bacterium and $N^P = 1000$ phage particles in a fully periodic, cubic simulation domain with box length $L = 16$ μm. Since all forces of our fluid–particle coupling scheme add to zero, the total momentum of the system remains at zero and no boundaries are necessary to keep the fluid at rest. When the bacterium moves forward, the fluid moves in the opposite direction with the same momentum—but since there is much more fluid mass than bacterium mass in the simulation box, the fluid center of mass remains nearly at rest. The volume fraction of phages $\phi = N^P 4\pi(r^P)^3/3L^3 \approx 10^{-4}$, is very low, so we expect any hydrodynamic interactions between them to be negligible. Moreover, in the ESI† we present evidence that there are no appreciable finite-size effects associated with the size of the simulation domain. We set the encounter distance $d_{enc} = r^P = 50$ nm; the time scale for phage diffusion across this distance is $\tau_{cross} \sim {d_{enc}}^2/D^P \approx 6 \times 10^{-4}$ s, so we choose the $\Delta t = 1 \times 10^{-4}$ s to adequately register phage encounters.

Each simulation is repeated $N^{ensemble}$ times with different seeds, *i.e.*, different initial conditions and noise realisations, to obtain the standard error of the mean of the quantities reported below. We choose $N^{ensemble} \geq 5$, the exact numbers for each reported result can be found in the data set[43] that accompanies this work.

3 Results

Before considering interactions with phages, we first verify that our simulation approach recapitulates the far-field dipolar flow field characteristic of swimming flagellated bacteria.[11,16] This is indeed the case, as shown in Fig. 2, which shows the fluid flow field in the laboratory frame of reference; furthermore, as shown in the ESI,† the fluid velocity magnitude v decays with distance r away from the cell as $\sim 1/r^2$, as predicted by theory. Importantly, while the bacterium moves in the positive z-direction, our model for the flagellum–fluid interaction leads to fluid motion in the negative z-direction inside the flagellum, with swimming being force-free overall.

Having established that our simulations reproduce this characteristic dipolar flow field, we next investigate what its implications are for attachment by phages. We emphasize that while the physics of direct phage–bacterium interactions happens on the scale of the phages, smaller than the grid size used for modeling the fluid flows, a key strength of our coupled molecular dynamics and lattice Boltzmann approach is that these direct phage–bacterium interactions are not influenced by the fluid simulation; instead, they are explicitly treated by our molecular dynamics approach over the encounter distance $d_{enc} = r^P = 50$ nm, much smaller than the lattice Boltzmann grid

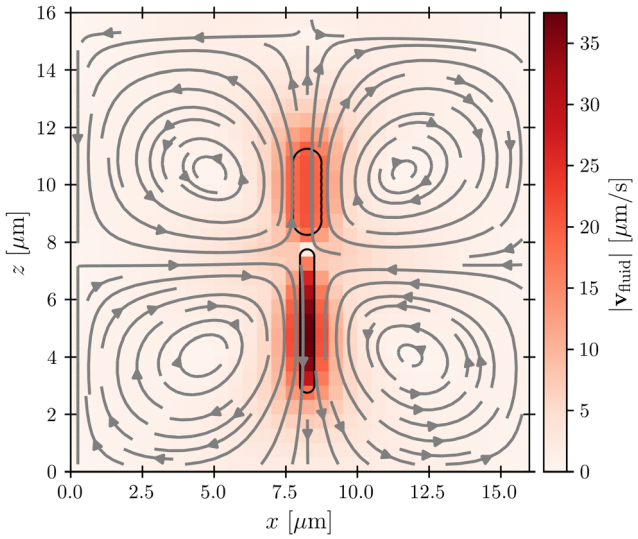

Fig. 2 Cross-section through the dipolar flow field generated by a swimming bacterium, in the stationary lab frame of reference. This representative example is for the case of v_{swim} = 20 μm s^{-1} in the absence of thermal noise in the lab frame. Color scale and arrows show the magnitude and orientation of the local fluid velocity, respectively. The upper and lower black outlines show the cell body and flagellum, respectively; the cell is swimming in the +z direction.

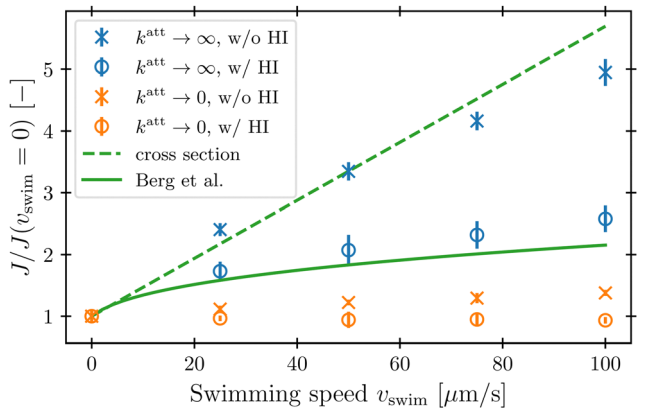

Fig. 3 Hydrodynamic interactions (HI) suppress the increase in phage attachment rate on the cell body with swimming speed. The attachment rate J integrated over the cell body is computed from our simulations and normalized by its value when the bacterium is not swimming. Blue and orange points show the cases of rapidly- or slowly-attaching phages, respectively. Error bars represent the standard error of the mean over statistically independent simulations. Dashed green line corresponds to a model of rapid phage attachment through diffusion and uptake by the cell body cross section, neglecting HI. Solid green line shows the prediction of Berg and Purcell from a more simplified continuum model of a driven spherical bacterium.

size. Thus, our approach treats both the large-scale features of fluid flows that advect phages—which vary on a much larger scale that is comparable to the size of the bacterium and much larger than the lattice Boltzmann grid cell—as well as the small-scale features of phage–bacteria interactions. As described below, we use these simulations to examine phage interactions first with the cell body, then with the flagellum.

3.1 Phage attachment to the cell body

To characterize how bacterial swimming and the associated hydrodynamic interactions (HI) influence how phages attach to the cell body, we compute the attachment rate J over a broad range of representative swimming speeds v_{swim}, for a broad range of k^{att}, with or without HI included. Our results are presented in Fig. 3 for the limiting cases of $k^{\text{att}} \to 0$ and $k^{\text{att}} \to \infty$ for clarity; the intermediate values of k^{att} monotonically interpolate between these cases, as shown in the ESI.†

We first consider the case of $k^{\text{att}} \to \infty$. In the absence of HI, J increases approximately linearly with v_{swim} (blue ×, Fig. 3), as suggested previously.[10] Indeed, without HI, we expect that $J/c_0 \approx 4\pi D^{\text{P}} r_{\text{eq}} + \pi r_{\text{eq}}^2 v_{\text{swim}}$; here, the first term on the right hand side describes the flux of a diffusive species into a spherical, stationary, perfect absorber[53] and is given by the solution of eqn (13) with $v_{\text{swim}} = 0$, and the second term takes the motion of the absorber into account by calculating the rate at which its cross section explores the volume filled with a constant number density of phages that are absorbed upon contact. As shown by the dashed green line in Fig. 3, this prediction agrees well with our simulation results.

Incorporating HI strongly suppresses attachment by phages, however. While J still increases monotonically with v_{swim}, the magnitude of this increase is considerably lessened by hydrodynamics (blue ○, Fig. 3)—indeed, by as much as twofold at the largest swimming speed tested. Why is this the case?

Close inspection of the flow field around the cell body provides a clue: as shown in Fig. 2, the no-slip boundary condition on the cell body surface causes a region of fluid in its immediate vicinity to be dragged along with it as it swims. We expect that this region also advects surrounding phages along with the cell, pushing them away from its forward-facing "head"; consequently, these phages must rely primarily on passive thermal diffusion to cross this region and successfully attach to the cell, independent of the bacterial swimming speed.

This effect is more clearly visualized in the reference frame that moves along with the bacterium. The relative flow field given by $\mathbf{v}_{\text{fl}}^* = \mathbf{v}_{\text{fl}} - v_{\text{swim}}\hat{\mathbf{e}}$, where the asterisk denotes quantities measured in this comoving frame, is shown in Fig. 4. We quantify the relative importance of phage advection and diffusion using the local Péclet number $\text{Pe}^*_{\text{phage}}(\mathbf{r}) \equiv |\mathbf{v}_{\text{fl}}^*(\mathbf{r})| r_{\text{body}}/D^{\text{P}}$ defined in this comoving frame; the iso-line of $\text{Pe}^*_{\text{phage}}(\mathbf{r}) = 1$ is shown by the dashed line. As expected, within the region bordered by the dashed line, the fluid is nearly at relative rest and $\text{Pe}^*_{\text{phage}}(\mathbf{r}) < 1$—confirming that any phages contained therein must rely primarily on thermal diffusion to attach to the cell body. Any enhancement in the phage attachment rate arising from bacterial swimming is therefore suppressed by this "protective shield" of fluid that surrounds the cell body.

This hydrodynamic effect manifests as $k^{\text{att}} \to 0$, as well. When HI are not included, the swimming bacterium is not protected by the "shield" of quiescent fluid discussed above. Instead, as it swims, the cell collects and accumulates phages at its head, and J again increases approximately linearly with

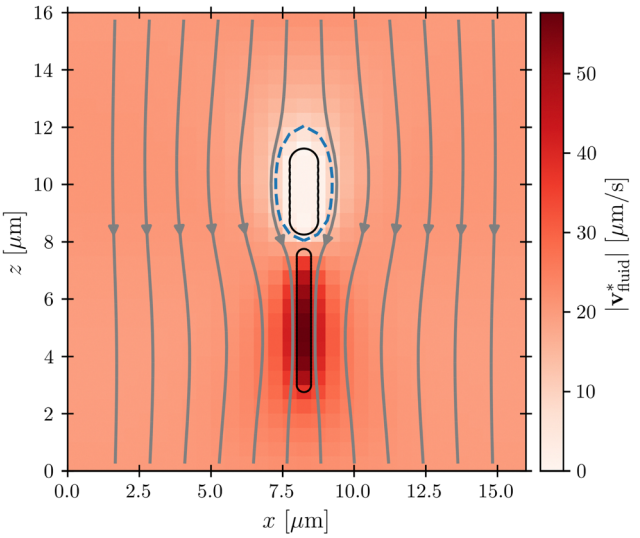

Fig. 4 Cross-section through the dipolar flow field generated by a swimming bacterium, in the cell's moving frame of reference. The image shows the same flow field as in Fig. 2, but in the comoving frame. The cell is swimming in the +z direction. The blue dashed line marks $\text{Pe}^*_{\text{phage}} = 1$.

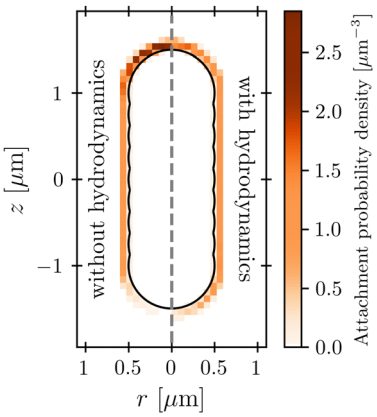

Fig. 5 Hydrodynamic interactions cause phages to be advected away from the head of the cell. Color scale shows the probability density of phage attachment over the surface of the cell body, for the example of $v_{\text{swim}} = 100$ μm s^{-1} and $k^{\text{att}} \to 0$. The cell is swimming in the +z direction. Without hydrodynamics, phages accumulate at its head, whereas when hydrodynamics are incorporated, the flow field established by swimming makes the distribution of attachment sites more uniform along the cell body.

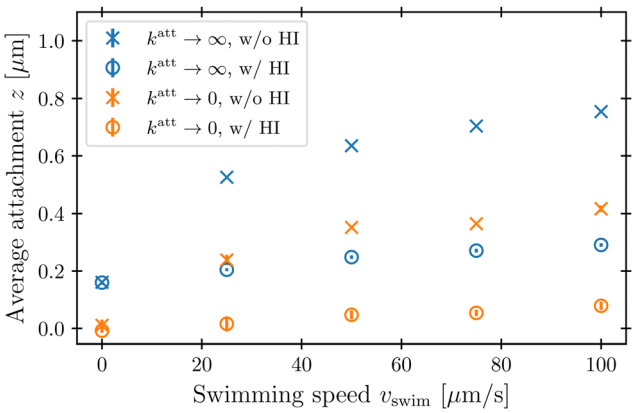

Fig. 6 Hydrodynamic interactions cause phages to be advected away from the head of the cell. Symbols show the average position of phage attachment positions along the bacterial symmetry axis relative to the cell body center. An average of $z > 0$ means the attachment probability density is shifted towards the head of the cell. Blue and orange points show the cases of $k^{\text{att}} \to \infty$ and $k^{\text{att}} \to 0$, respectively. Error bars represent the standard error of the mean over statistically independent simulations, and are sometimes smaller than the symbol size.

v_{swim}, as shown by the orange × in Fig. 3. In this case, the swimming bacterium does not appreciably remove contacting phages from the fluid, whereas in the case of $k^{\text{att}} \to \infty$, phages are locally depleted from the vicinity of the cell upon contact and attachment. Therefore, the dependence of J on v_{swim} is more modest for phages with $k^{\text{att}} \to 0$; indeed, when HI are included, there is no measurable dependence of J on v_{swim} (orange ○, Fig. 3).

The protective influence of the hydrodynamic "shield" is also apparent in the spatial distribution of phage attachment over the cell body, shown for the example of $v_{\text{swim}} = 100$ μm s^{-1} and $k^{\text{att}} \to 0$ in Fig. 5; the corresponding distributions for a range of other swimming speeds are shown in the ESI.† As expected, without HI (left panel), phage attachment occurs preferentially at the head of the cell. However, HI push phages away from the head of the cell, causing attachment to be distributed more uniformly around the cell body (right panel). Fig. 6 quantifies this difference for all the simulation conditions tested using the average z-position of phage attachment relative to the cell body center of mass, *i.e.*, the first moment of the attachment probability density. Again, as shown by the difference between × and ○ symbols, HI reduce the asymmetry of phage attachment for both $k^{\text{att}} \to 0$ and $k^{\text{att}} \to \infty$ over all swimming speeds tested.

In their classic paper,[13] Berg and Purcell did not consider the elongated shape of a swimming bacterium, the distinction between the cell body and flagellum, or the dipolar flow field established by swimming. Nevertheless, using a more simplified continuum model of an externally-forced sphere, they intuited the protective hydrodynamic effect uncovered by our simulations, noting that "The molecules [or in our case, phages] in front of the cell are carried out of its way along with the fluid it must push aside to move. The cell carries with it a layer of liquid that is practically stationary in its frame of reference. Every molecule [or phage] that reaches the surface of the cell must cross this layer by diffusion." Remarkably, despite the simplifications made in their work, Berg and Purcell's prediction for the attachment rate (solid green curve, Fig. 3) shows excellent agreement with the results of our more detailed simulations (blue ○). One may not expect this agreement *a priori* given the marked difference between the actual dipolar flow field established by the swimming cell and the approximation used by Berg and Purcell. However, our results show that the essential qualitative feature of the low $\text{Pe}^*_{\text{phage}}$ region is independent of the shape and propulsion mechanism of the bacterium, justifying their simplifying assumptions

a posteriori—but only for the case of the cell body. As we show in the next section, we find dramatically different behavior for the bacterial flagellum.

3.2 Phage attachment to the flagellum

While the cell body drags a protective region of fluid with it, the flagellum does not. Instead, because it is permeable to and exerts a force on the fluid, $\mathrm{Pe}^*_{\mathrm{phage}} \gg 1$ especially in the immediate vicinity of the flagellum, as seen by the dark red region of Fig. 4. As a result, we expect that hydrodynamic interactions are not protective as for the cell body, but instead, promote attachment to the flagellum. Our simulations confirm this expectation, as shown in Fig. 7.

Unlike the case of the cell body, HI greatly increase the flagellar attachment rate, as seen by comparing the ○ and × points in Fig. 7(A)—indeed, by nearly twofold at the largest swimming speed tested. In the absence of HI, J only increases marginally with v_{swim} for $k^{\mathrm{att}} \to \infty$. It even decreases with v_{swim} for $k^{\mathrm{att}} \to 0$, due to the cell body pushing phages radially outward upon contact. However, when HI are taken into account, the flagellum pumps in phage-laden fluid from the sides of the cell body and moves it through the space occupied by the flagellar bundle. Therefore, the volume of fluid coming in contact with the flagellum, and thus phage attachment, increases with v_{swim}. Moreover, because the fluid is pumped along the $-\hat{\mathbf{e}}$ direction, we expect that phage attachment is more likely to occur at the forward end of the flagellum with increasing v_{swim}. Inspecting the spatial distribution of phage attachment along the flagellum confirms this expectation, as shown for the example of $v_{\mathrm{swim}} = 100\ \mu\mathrm{m\ s}^{-1}$ and $k^{\mathrm{att}} \to 0$ in Fig. 7(B), and quantified for all the simulation conditions tested in Fig. 7(C).

3.3 Overall attachment rate

Our simulations have revealed that hydrodynamic interactions suppress phage attachment to the cell body and conversely promote attachment to the flagellum. How do these effects compete in determining the overall phage attachment rate integrated over the entire cell body and flagellum? Inspecting the flow field in the reference frame that moves along with the bacterium (Fig. 4) suggests that these effects should nearly cancel each other out, since the fluid streamlines immediately in front of the cell body bend around it and then become refocused within the flagellum. Therefore, phages that would have attached to the cell body in the absence of HI are instead advected by the fluid to later attach to the flagellum, instead—causing the overall attachment rate to be unaffected. This expectation is borne out by the simulations, as shown in Fig. 8: hydrodynamic interactions do not appreciably influence the overall attachment rate, just the position of phage attachment. Taken together, these results highlight the importance of

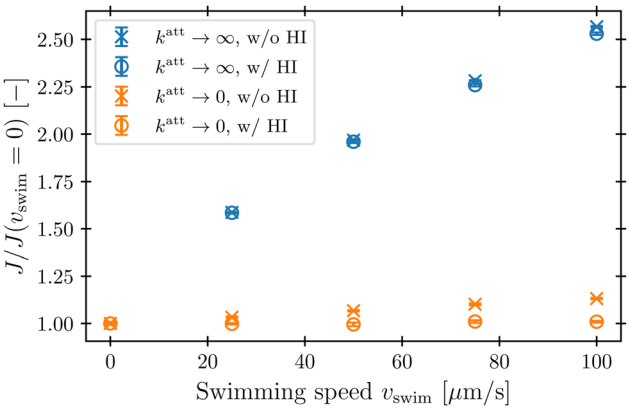

Fig. 8 Hydrodynamic interactions do not appreciably influence the overall phage attachment rate. The attachment rate J integrated over the entire bacterium comprising cell body and flagellum is computed from our simulations for varying v_{swim} and normalized by its value when the bacterium is not swimming. Blue and orange points show the cases of $k^{\mathrm{att}} \to \infty$ and $k^{\mathrm{att}} \to 0$, respectively. Error bars represent the standard error of the mean over statistically independent simulations.

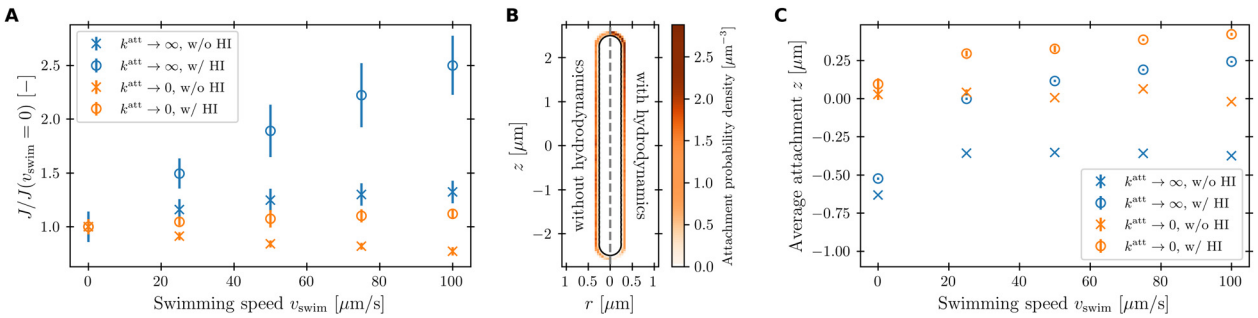

Fig. 7 Hydrodynamic interactions promote phage attachment to the flagellum. (A) The attachment rate J integrated over the flagellum is computed from our simulations for varying v_{swim} and normalized by its value when the bacterium is not swimming. (B) Color scale shows the probability density of phage attachment over the surface of the flagellum, for the example of $v_{\mathrm{swim}} = 100\ \mu\mathrm{m\ s}^{-1}$ and $k^{\mathrm{att}} \to 0$. The cell is swimming in the $+z$ direction. When hydrodynamics are incorporated, fluid pumping by the flagellum along the $-z$ direction drives phage attachment near the forward end of the flagellum. (C) Symbols show the average position of phage attachment positions along the bacterial symmetry axis relative to the flagellum center. An average of $z > 0$ means the attachment probability density is shifted towards the forward end of the flagellum. For $k^{\mathrm{att}} \to \infty$, the attachment is shifted into the negative direction at $v_{\mathrm{swim}} = 0$ because the cell body depletes the region in front of the flagellum of phages. Error bars in (A) and (C) represent the standard error of the mean over statistically independent simulations. Blue and orange points show the cases of $k^{\mathrm{att}} \to \infty$ and $k^{\mathrm{att}} \to 0$, respectively.

considering spatial variations of attachment fluxes along the surface of the cell, not just their overall sum, which masks these variations.

4 Conclusions

Using coarse-grained molecular dynamics simulations of a swimming bacterium that explicitly treat its cell body and flagellum separately, with hydrodynamic interactions incorporated *via* coupling to a lattice Boltzmann fluid, our work has shed new light on the influence of swimming on attachment by phages. We find that while swimming increases the rate at which phages attach to both the cell body and flagellar propeller, hydrodynamic interactions strongly suppress this increase at the cell body, but conversely enhance this increase at the flagellar bundle. This difference in attachment arises from the characteristic dipolar flow field generated by a swimming bacterium, which advects phages away from the cell body, but pumps phage-laden fluid into the flagellum. Hence, while our results corroborate the findings of Berg and Purcell for the cell body, our work provides a counterpoint to their conclusion that ''in a uniform medium motility cannot significantly increase the cell's acquisition of material.'' (In our case, ''material'' refers to external phages, although our results may also apply to cellular uptake of chemical species like nutrients and antibiotics[54]). Experimentally testing these predictions—*e.g.*, by combining direct visualization of phage attachment[55] with optical trapping of swimming cells[56]—will be an important direction for future work.

While in the main text we focused on the case of pusher-type bacteria, many other microswimmers (*e.g.*, *Chlamydomonas reinhardtii*) are pullers: their flagellum is at the front of the cell body, not the rear, and as a result, they generate a similar flow field to that of a pusher, but with opposite flow directions.[57] To explore the generality of our findings, we also perform all our simulations with a puller-type swimmer with $l_{\mathrm{dipole}} = 5$ μm, which is equivalent to reversing the swim force $\mathbf{F}^{\mathrm{swim}}$ and correspondingly redefining the notions of ''forward'' and ''backward''. In this case, our results (shown in the ESI†) point to a similar overall conclusion as for pushers: while the fluid flow generated by swimming helps to protect the cell body from phages, it promotes phage attachment at the flagellum. Building on our work, it will be interesting to investigate how hydrodynamics influence interactions with phages for microswimmers that use other forms of swimming. Another related direction for future inquiry will be to investigate how the flows generated by collectives of microswimmers,[58] *versus* the individuals considered here, influence interactions with phages.

Our model takes a step toward capturing the essential biophysical processes underlying the interactions between phage and swimming bacteria, and necessarily involved some simplifying assumptions and approximations. For example, in reality, the surfaces of individual flagella in a bundle are no-slip boundaries; therefore, a region of small Péclet number surrounds each flagellum over which phages must diffuse, following a similar argument to that we made for the cell body. However, because the flagellar bundle consists of many individual flagella moving at large speeds compared to the swim speed of the cell body, the small-Pe region around each flagellum is much smaller than that around the cell body. The flows inside the bundle are also highly complex and time-dependent, potentially increasing the mixing of phages that enter the bundle and the likelihood of contact. Our modelling approach simplifies these complex interactions by coarse-graining the fast moving, small flagella into a larger solid, permeable object representing the entire bundle. Importantly, because inside the bundle the aforementioned factors increase the likelihood of phage attachment, the rate-limiting step to attachment is the approach of a phage from the exterior to the bundle itself, mediated by larger-scale hydrodynamics—which are captured by our coarse-grained model. Therefore, while a model with explicitly-resolved flagella could yield attachment rates that are slightly different from ours, because the rate-limiting step to attachment is phage transport from the exterior of the cell to the surface of the flagella—*versus* the subsequent step of contacting an individual flagellum—we expect that our central findings would be the same in such an explicitly-resolved model. Exploring these details will be a useful direction for future work.

Another simplification we made is to model phage–bacterium interactions as being short-ranged and purely-repulsive; exploring the influence of more sophisticated microscopic interactions will be another useful direction for further research. We do not expect that our central findings will change in this case, however: our coarse-grained treatment subsumes all these complex microscopic interactions into the lumped rate k^{att}, and as shown in the ESI,† the conclusions of our work are robust to changes in the exact value of this parameter.

Altogether, our findings highlight the pivotal influence of hydrodynamics on the interactions between bacteria and phages, as well as other diffusible species—*e.g.*, nutrients, toxins, or signalling molecules—in microbial environments. They also provide a new perspective on the biophysical trade-offs associated with bacterial swimming. While swimming can be beneficial by enabling bacteria to escape from harmful environments, find new resources, and colonize new terrain, it can also be costly—not only because of the additional energy it requires of the cell, but also because it is often thought to increase the probability of encountering surrounding phages. Our results demonstrate that this latter cost is not appreciable for the cell body, due to the protective ''shield'' of fluid established by hydrodynamics, but is appreciable for the flagellar bundle, which pumps surrounding phages in. We conjecture that this may in part be why many phages have, over billions of years of evolution, developed ways to exploit bacterial swimming for their benefit by targeting the flagellum.[18,19] Swimming bacteria may, in turn, have evolved localised defence countermeasures against phage infection such as through modification of specific surface receptors or production of outer membrane vesicles as decoys.[59] Investigating how these biological and chemical processes, combined with the hydrodynamic effects

illuminated by our work, influence phage–bacteria interactions will be a useful avenue for future research.

Data and code availability

The data that support the findings of this study as well as the source code are available in ref. 43.

Author contributions

C. L. performed all simulations and theoretical calculations; C. L., C. H., and S. S. D. designed the simulations, analyzed the data, discussed the results and implications, and wrote the manuscript; S. S. D. designed and supervised the overall project.

Conflicts of interest

There are no conflicts to declare.

Acknowledgements

We thank the Visiting Student Research Collaborator (VSRC) program of the Graduate School at Princeton for enabling C. L. to visit the Datta Lab and conduct this research, as well as funding support by the Deutsche Forschungsgemeinschaft (DFG, German Research Foundation) under project number 327154368-SFB 1313 and under Germany's Excellence Strategy EXC 2075 – 390740016. The simulations were performed on computational resources managed and supported by Princeton Research Computing, a consortium of groups including the Princeton Institute for Computational Science and Engineering (PICSciE) and the Office of Information Technology's High Performance Computing Center and Visualization Laboratory at Princeton University. It is a pleasure to thank Ido Golding and Ned Wingreen for useful discussions, and Chris Browne for helpful comments on the manuscript.

Notes and references

1 R. W. Hendrix, M. C. M. Smith, R. N. Burns, M. E. Ford and G. F. Hatfull, *Proc. Natl. Acad. Sci. U. S. A.*, 1999, **96**, 2192–2197.
2 A. Mushegian, *J. Bacteriol.*, 2020, **202**, 10–1128.
3 C. A. Suttle, *Nature*, 2005, **437**, 356–361.
4 A. Chevallereau, B. J. Pons, S. van Houte and E. R. Westra, *Nat. Rev. Microbiol.*, 2022, **20**, 49–62.
5 B. Koskella, C. A. Hernandez and R. M. Wheatley, *Annu. Rev. Virol.*, 2022, **9**, 57–78.
6 M. Breitbart, C. Bonnain, K. Malki and N. Sawaya, *Nat. Microbiol.*, 2018, **3**, 754–766.
7 S. A. Strathdee, G. F. Hatfull, V. K. Mutalik and R. T. Schooley, *Cell*, 2023, **186**, 17–31.
8 H. G. Hampton, B. N. Watson and P. C. Fineran, *Nature*, 2020, **577**, 327–336.
9 S. T. Abedon, *Antibiotics*, 2023, **12**, 723.
10 K. L. Joiner, A. Baljon, J. Barr, F. Rohwer and A. Luque, *Sci. Rep.*, 2019, **9**, 1–12.
11 K. Drescher, J. Dunkel, L. H. Cisneros, S. Ganguly and R. E. Goldstein, *Proc. Natl. Acad. Sci. U. S. A.*, 2011, **108**, 10940–10945.
12 A. J. Mathijssen, R. Jeanneret and M. Polin, *Phys. Rev. Fluids*, 2018, **3**, 033103.
13 H. Berg and E. Purcell, *Biophys. J.*, 1977, **20**, 193–219.
14 S. Friedlander, *AIChE J.*, 1957, **3**, 43–48.
15 A. Acrivos and T. D. Taylor, *Phys. Fluids*, 1962, **5**, 387–394.
16 E. Lauga, *Annu. Rev. Fluid Mech.*, 2016, **48**, 105–130.
17 S. E. Spagnolie and E. Lauga, *J. Fluid Mech.*, 2012, **700**, 105–147.
18 P. Katsamba and E. Lauga, *Phys. Rev. Fluids*, 2019, **4**, 013101.
19 N. C. Esteves and B. E. Scharf, *Int. J. Mol. Sci.*, 2022, **23**, 7084.
20 A. Patteson, A. Gopinath, M. Goulian and P. Arratia, *Sci. Rep.*, 2015, **5**, 15761.
21 J. P. Binagia and E. S. Shaqfeh, *Phys. Rev. Fluids*, 2021, **6**, 053301.
22 K. D. Housiadas, J. P. Binagia and E. S. Shaqfeh, *J. Fluid Mech.*, 2021, **911**, A16.
23 J. P. Binagia, A. Phoa, K. D. Housiadas and E. S. Shaqfeh, *J. Fluid Mech.*, 2020, **900**, A4.
24 J. A. Puente-Velázquez, F. A. Godnez, E. Lauga and R. Zenit, *Microfluid. Nanofluid.*, 2019, **23**, 1–7.
25 L. Zhu, E. Lauga and L. Brandt, *Phys. Fluids*, 2012, **24**, 051902.
26 L. W. Rogowski, J. Ali, X. Zhang, J. N. Wilking, H. C. Fu and M. J. Kim, *Nat. Commun.*, 2021, **12**, 1116.
27 V. A. Martinez, J. Schwarz-Linek, M. Reufer, L. G. Wilson, A. N. Morozov and W. C. Poon, *Proc. Natl. Acad. Sci. U. S. A.*, 2014, **111**, 17771–17776.
28 Z. Qu and K. S. Breuer, *Phys. Rev. Fluids*, 2020, **5**, 073103.
29 Y. Zhang, G. Li and A. M. Ardekani, *Phys. Rev. Fluids*, 2018, **3**, 023101.
30 S. Kamdar, S. Shin, P. Leishangthem, L. F. Francis, X. Xu and X. Cheng, *Nature*, 2022, **603**, 819–823.
31 A. Martínez-Calvo, C. Trenado-Yuste and S. S. Datta, *Out-of-equilibrium Soft Matter*, The Royal Society of Chemistry, 2023, ch. 5, pp. 151–218.
32 T. Krüger, H. Kusumaatmaja, A. Kuzmin, O. Shardt, G. Silva and E. M. Viggen, *The Lattice Boltzmann Method: Principles and Practice*, Springer International Publishing, 2017.
33 B. Dünweg, U. D. Schiller and A. J. Ladd, *Phys. Rev. E: Stat., Nonlinear, Soft Matter Phys.*, 2007, **76**, 036704.
34 P. Ahlrichs and B. Dünweg, *J. Chem. Phys.*, 1999, **111**, 8225–8239.
35 J. de Graaf, H. Menke, A. J. Mathijssen, M. Fabritius, C. Holm and T. N. Shendruk, *J. Chem. Phys.*, 2016, **144**, 134106.
36 M. Lee, K. Szuttor and C. Holm, *J. Chem. Phys.*, 2019, **150**, 174111.
37 M. Lee, C. Lohrmann, K. Szuttor, H. Auradou and C. Holm, *Soft Matter*, 2021, **17**, 893–902.
38 C. Lohrmann and C. Holm, *Phys. Rev. E*, 2023, **108**, 054401.

39 J. D. Weeks, D. Chandler and H. C. Andersen, *J. Chem. Phys.*, 1971, **54**, 5237–5247.
40 F. Weik, R. Weeber, K. Szuttor, K. Breitsprecher, J. de Graaf, M. Kuron, J. Landsgesell, H. Menke, D. Sean and C. Holm, *Eur. Phys. J.: Spec. Top.*, 2019, **227**, 1789–1816.
41 M. Bauer, S. Eibl, C. Godenschwager, N. Kohl, M. Kuron, C. Rettinger, F. Schornbaum, C. Schwarzmeier, D. Thönnes and H. Köstler, *et al.*, *Comput. Math. Phys.*, 2021, **81**, 478–501.
42 C. Godenschwager, F. Schornbaum, M. Bauer, H. Köstler and U. Rüde, *Proceedings of the International Conference on High Performance Computing, Networking, Storage and Analysis*, 2013, pp. 1–12.
43 C. Lohrmann and C. Holm, *Replication Data for: Lohrmann, Holm, Datta: Influence of bacterial motility and hydrodynamics on phage bacteria encounters*, 2023, DOI: **10.18419/darus-3836**.
44 M. Schwartz, *J. Mol. Biol.*, 1976, **103**, 521–536.
45 Z. J. Storms and D. Sauvageau, *Virology*, 2015, **485**, 355–362.
46 A. Logg and G. N. Wells, *ACM Trans. Math. Software*, 2010, **37**, 1–28.
47 H.-W. Ackermann and H. Krisch, *Arch. Virol.*, 1997, **142**, 2329–2345.
48 J. J. Barr, R. Auro, N. Sam-Soon, S. Kassegne, G. Peters, N. Bonilla, M. Hatay, S. Mourtada, B. Bailey, M. Youle, B. Felts, A. Baljon, J. Nulton, P. Salamon and F. Rohwer, *Proc. Natl. Acad. Sci. U. S. A.*, 2015, **112**, 13675–13680.
49 J. Schwarz-Linek, J. Arlt, A. Jepson, A. Dawson, T. Vissers, D. Miroli, T. Pilizota, V. A. Martinez and W. C. Poon, *Colloids Surf., B*, 2016, **137**, 2–16.
50 A. Andino and I. Hanning, *et al.*, *Sci. World J.*, 2015, **2015**, 520179.
51 S. Datta and D. K. Srivastava, *Proc. Math. Sci.*, 1999, **109**, 441–452.
52 F. Perrin, *J. Phys. Radium*, 1934, **5**, 497–511.
53 M. v Smoluchowski, *Z. Phys. Chem.*, 1918, **92**, 129–168.
54 R. C. Coelho, N. A. Araújo and M. M. T. da Gama, *Soft Matter*, 2022, **18**, 7642–7653.
55 E. Rothenberg, L. A. Sepúlveda, S. O. Skinner, L. Zeng, P. R. Selvin and I. Golding, *Biophys. J.*, 2011, **100**, 2875–2882.
56 T. L. Min, P. J. Mears, L. M. Chubiz, C. V. Rao, I. Golding and Y. R. Chemla, *Nat. Methods*, 2009, **6**, 831–835.
57 J. Elgeti, R. G. Winkler and G. Gompper, *Rep. Prog. Phys.*, 2015, **78**, 056601.
58 A. J. Mathijssen, F. Guzmán-Lastra, A. Kaiser and H. Löwen, *Phys. Rev. Lett.*, 2018, **121**, 248101.
59 K. D. Seed, *PLoS Pathog.*, 2015, **11**, e1004847.